

Electrically Controllable Single-Point Covalent Functionalization of Spin-Cast Carbon-Nanotube Field-Effect Transistor Arrays

Yoonhee Lee,^{†,||} Scott M. Trocchia,^{†,||} Steven B. Warren,[‡] Erik F. Young,[†] Sefi Vernick,[§] and Kenneth L. Shepard^{*,†}

[†]Department of Electrical Engineering, Columbia University, New York, New York 10027, United States

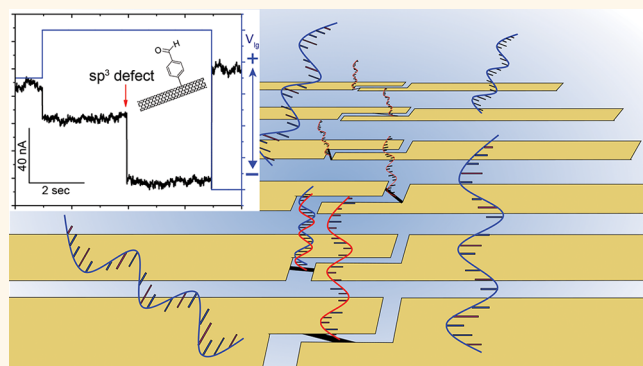
[‡]Pacific Biosciences, Menlo Park, California 94025, United States

[§]Agricultural Research Organization, Volcani Center, Institute of Agricultural Engineering, Bet Dagan, Israel

Supporting Information

ABSTRACT: Single-point-functionalized carbon-nanotube field-effect transistors (CNTFETs) have been used to sense conformational changes and binding events in protein and nucleic acid structures from intrinsic molecular charge. The key to utilizing these devices as single-molecule sensors is the ability to attach a single probe molecule to an individual device. In contrast, with noncovalent attachment approaches such as those based on van der Waals interactions, covalent attachment approaches generally deliver higher stability but have traditionally been more difficult to control, resulting in low yield. Here, we present a single-point-functionalization method for CNTFET arrays based on electrochemical control of a diazonium reaction to create sp^3 defects, combined with a scalable spin-casting method for fabricating large arrays of devices on arbitrary substrates. Attachment of probe DNA to the functionalized device enables single-molecule detection of DNA hybridization with complementary target, verifying the single-point functionalization. Overall, this method enables single-point defect generation with 80% yield.

KEYWORDS: carbon nanotube, spin-cast, wafer scale, CNTFET array, smFET, diazonium, single-point defect, DNA melting



Single-molecule measurement techniques enable quantitative measurement of intra- and intermolecular interaction kinetics. The strengths of these methods include their ability to report rare intermediate states along reaction pathways which are otherwise averaged out in ensemble measurements and the ability to yield information on the biological mechanism underlying the interaction. The information from these measurements has provided detailed information on protein structural dynamics,^{1,2} DNA hybridization,³ and DNA and protein recognition,⁴ providing insights into chemical, mechanical, and structural characteristics of biomolecules. In the case of genomic analysis,^{5–7} single molecule experiments allow quantitative detection of genomic target without labeling or amplification.

The limitations of current single-molecule measurement technologies include short observation times and narrow bandwidth in transducer and measurement electronics. The observation time in fluorescence-based approaches, such as single-molecule Förster resonance energy transfer (smFRET), is limited by photobleaching of fluorophores. Measurement

bandwidths are limited by achievable signal-to-noise ratios (SNRs). Fluorescence emission of single optical reporters is typically on the scale of only 1000–4000 photons/s under normal excitation powers,^{8,9} requiring integration times in imagers on a millisecond time scale. Mechanical single-molecule approaches offer longer observation times, and recent high-speed single molecule force spectroscopy techniques have achieved microsecond time scales.^{10,11} However, cantilevers must be attached to the molecules in question, and measurement scaling to massively parallel formats is not easily achieved. Both optical and mechanical approaches require sophisticated and expensive instrumentation, impeding broader application of these tools.

Point-functionalized carbon nanotube (CNT) devices have emerged as an all-electronic, label-free, single-molecule

Received: April 24, 2018

Accepted: September 27, 2018

Published: September 27, 2018



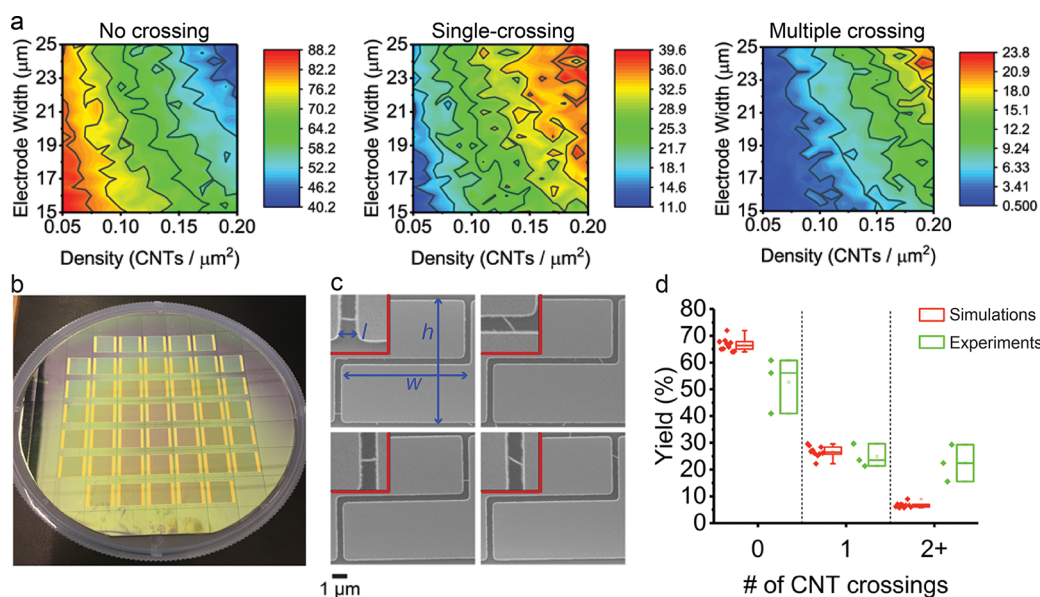


Figure 1. (a) Simulated percentages of zero, single, and multiple nanotube crossings are depicted. Five hundred electrode pairs are simulated for each density and width pairing. (b) Top-down photograph of fully processed 100 mm Si/SiO₂ wafer. (c) Representative SEM scans of single-nanotube crossings. Electrode width (w), gap (l), and height (h) are noted. Insets in each panel show a more magnified view of the nanotube crossing. (d) Statistical comparison of simulated and experimental yields for spin-cast nanotubes. Simulations were run 10 times with a surface concentration of 0.13 CNT/ μm^2 and an electrode width of 20 μm . Experimental yields were computed from SEM images of all electrode pairs on three chips from the same wafer.

detection platform.¹² The single-point-functionalized CNT field-effect transistor (CNTFET), which we refer to here as the single-molecule field-effect transistor (smFET), is characterized by a conductance that is sensitive to charges localized within a few debye lengths of a point defect that is generated on the CNT sidewall.^{13,14} Systems employing smFETs transduce high-rate random telegraph signal (RTS) fluctuations directly with bandwidths in excess of 1 MHz over a virtually unlimited observation time.¹⁵ Single-molecule experiments with smFETs have included studies of the dynamics of DNA hybridization,⁵ G-quadruplex conformation changes,¹⁶ and lysozyme activity,¹⁷ and these findings harmonize with results from fluorescence-based and force-based experiments.

The scope of smFET applications has still been restricted by the low yield of fabrication. In particular, detailed statistics resulting from the ability to analyze data from many different devices is lacking. Large arrays of CNTFETs will enable parallelization and scale useful for many applications. CNTFET fabrication approaches generally involve fabrication of multiple devices on a single CNT grown by chemical vapor deposition (CVD),¹⁸ a technique that is not amenable to large-scale manufacturing since devices must be customized to exact nanotube placement.

An additional restriction to broader smFET use is inefficiency in the point functionalization of the FET channel. Transient, singular, noncovalent probe attachment have been pursued using pyrenes or porphyrins exploiting π - π -stacking of these molecules with the carbon rings of the CNT.^{19,20} Reuse of devices is possible in this case, since the attached probe can be removed at the cost of instability in the attachment. A covalent attachment strategy offers desirable permanent tethering of probe molecules as well as localization of charge-sensitivity for the device at the point of attachment.²¹ Covalent modification methods include aryl radical,²² nucleophilic, and electrophilic additions,^{23,24} which impart a measurable resistance change in the device by converting

carbon bonding from sp^2 to sp^3 orientation rather than by removing carbon atoms from the lattice. There have been a few attempts to regulate these reactions to produce a single sp^3 defect, either by employing nanowells^{5,16} or by controlling the potential between the CNT and the surrounding electrolyte^{15,25} during the chemical reaction. Confining conjugation chemistry with nanowells requires electron-beam patterning of a thin layer of resist to form a well in which the sp^3 reaction can occur. With nanowells as narrow as 20 nm, the yield for sp^3 defect generation has been close to 70%.¹⁶ However, this technique is not amenable to large-scale device production because of the required lithographic resolution for these wells. The electrochemical potential methods function by applying solution bias to promote or inhibit electron transfer between a charged moiety and the carbon nanotube lattice, and the associated electrical resistance change due to the addition of a single sp^3 defect has been argued to be on the order of $h/4e^2$.^{25,26} However, previous efforts at controlling these reactions have been limited by the inability to terminate the reaction reliably after single defect generation, reducing the yield of single defects.

In this study, we demonstrate a spin-cast method for fabricating large arrays of metal-contacted single nanotubes. These devices are converted to single-point-functionalized CNTFET by employing electrochemical reduction of aryl diazonium salts, which is controlled by applied potential with yields for single defects of better than 80%. The resultant devices are shown to be competent for genomic identification of 20-mer DNA targets employing a conjugated 20-mer probe DNA to the defect sites, achieving an average SNR of 2.4 ± 1.1 .

RESULTS AND DISCUSSION

Estimation of CNTFET Yield. Previous spin-cast efforts have utilized multiple deposition cycles to manipulate the thin-

film deposition of unbundled nanotubes from an air–liquid interface²⁷ or laminar flow at a liquid–liquid interface.²⁸ Deposition conditions are affected by multiple parameters, such as the flow velocity, surface pressure, or thin-film thickness, and it makes the manufacturing process difficult. Here, borrowing from commercial semiconductor fabrication processing, we use a single spin cycle to randomly place a dilute aqueous single-walled CNT (SWCNT) suspension across large wafer surfaces.

We performed simulations to understand better how spin-cast parameters affect the device yield. We model the expected number of nanotubes bridging electrode pairs as a function of both nanotube density and electrode width (w) at a fixed electrode gap (l) of $0.5\ \mu\text{m}$ (spacing between electrodes) and an electrode height (h) of $10\ \mu\text{m}$ (Figure S1 in Supporting Information). The nanotube solution used in this work is composed of a purified, commercially available unsorted SWCNT solution (<5% carbonaceous impurities).²⁹ The length of these nanotubes follows a log-normal distribution with a mean (μ) of $-0.36\ \mu\text{m}$ and a standard deviation (σ) of $0.60\ \mu\text{m}$, as characterized by scanning electron-beam microscopy (SEM) of more than 1200 spin-cast CNTs. The electrode gap (l) is chosen to be commensurate with this nanotube length distribution. The electrodes are designed as a zigzag shape to allow for CNT transits in both the horizontal and vertical directions. In the simulations, placement of nanotubes by spin-cast deposition is assumed to produce a continuous uniform probability distribution across the wafer.

Both higher nanotube density and wider electrodes are expected to result in a higher frequency of nanotube bridges between electrodes. Statistics are collected for 500 simulated electrode pairs, a nanotube density ranging from 0.05 to $0.25\ \text{CNT}/\mu\text{m}^2$, and electrode widths ranging between 5 and $25\ \mu\text{m}$. Figure 1a presents contour plots of the percentage of zero-nanotube, one-nanotube, and multiple nanotubes occurrences for an electrode pair as a function of both nanotube density and electrode width. The probability of precisely incorporating single nanotubes between a $20\ \mu\text{m}$ wide electrode pair is slightly higher than 30% for nanotube densities between 0.15 and $0.20\ \text{CNTs}/\mu\text{m}^2$. The theoretical maximum yield of single CNT crossings, dictated by Poisson statistics, is approximately 36% ($P(1) = 1/e$).

Wafer-Scale CNTFET Fabrication. For spin-coating, 1 – $2\ \text{mL}$ of a suspension (with a nanotube concentration of 1.6 to $2.5\ \mu\text{g}/\text{mL}$) is used to cover the entire surface of a $100\ \text{mm}$ silicon wafer with $285\ \text{nm}$ of thermal oxide on the surface, and the resulting surface concentration is $0.13 \pm 0.02\ \text{CNTs}/\mu\text{m}^2$, assessed from 11 SEM micrographs (with the field of view of $500\ \mu\text{m}^2$) of the wafer postspinning. Each wafer yields 45 chips ($11\ \text{mm}$ by $10\ \text{mm}$ size) (Figure 1b); each chip contains 280 pairs of source-drain electrical contacts ($w = 20\ \mu\text{m}$, $l = 0.5\ \mu\text{m}$, and $h = 10\ \mu\text{m}$). Representative micrographs of devices with single nanotube crossings, taken at various locations on a single die, are shown in Figure 1c. Simulations predict an average yield of zero-crossings of 65%, one-crossing of 27%, and multiple crossings of 8% for the same CNT surface concentration ($0.13\ \text{CNTs}/\mu\text{m}^2$) and electrode width employed in these experiments ($20\ \mu\text{m}$), compared with experimentally measured values of 53%, 25%, and 22%, respectively (Figure 1d). The experimental single-crossing yield, an important criterion for CNTFET fabrication, matches closely with simulation results. Nanotube bundling is not accounted for in these simulations.

To ensure that the CNT devices electrically conduct after all processing steps, current–voltage (I – V) characteristics of 1960 electrode pairs from seven chips are examined by applying back-gated voltage sweeps (V_{bg} , applied on the underlying silicon substrate) from -10 to $+10\ \text{V}$. Since solution-processed SWCNTs are composed of mixtures of metallic (m-SWCNTs) and p-type semiconducting nanotubes (s-SWCNTs), conductive devices are determined based on measured on-current (I_{on}) at $V_{\text{bg}} = -10\ \text{V}$ and a source-to-drain (V_{sd}) of $100\ \text{mV}$ (Figure S3 in Supporting Information). Conductive CNTFETs are defined by an I_{on} of at least $1.0\ \text{nA}$, and $67.4 \pm 9.9\%$ of electrode pairs are identified as nonconductive (Figure 2a). The remaining conducting devices

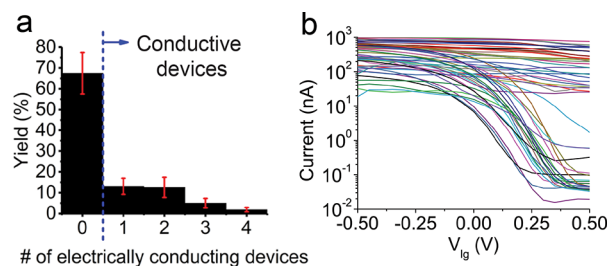


Figure 2. (a) Histograms of the number of electrically conducting devices across seven chips on one wafer. All zero crossings represent electrode pairs which did not conduct (even though they may have one or more nanotubes bridging them in the corresponding SEM image). SEM images are referenced to verify the presence of one, two, three, or four CNT crossings. Error bars are calculated from seven chips from the same wafer. (b) Electronic sweeps in sodium phosphate buffer solution ($100\ \text{mM}$, $\text{pH}\ 8.0$) of 49 single-crossing nanotube devices deposited on four separate chips. These devices not only have a single CNT bridge but also exceed threshold I_{on} values of $1\ \text{nA}$ in I – V_{lg} characteristics at $V_{\text{sd}} = 100\ \text{mV}$. Both semiconducting and metallic electrical behavior are evident.

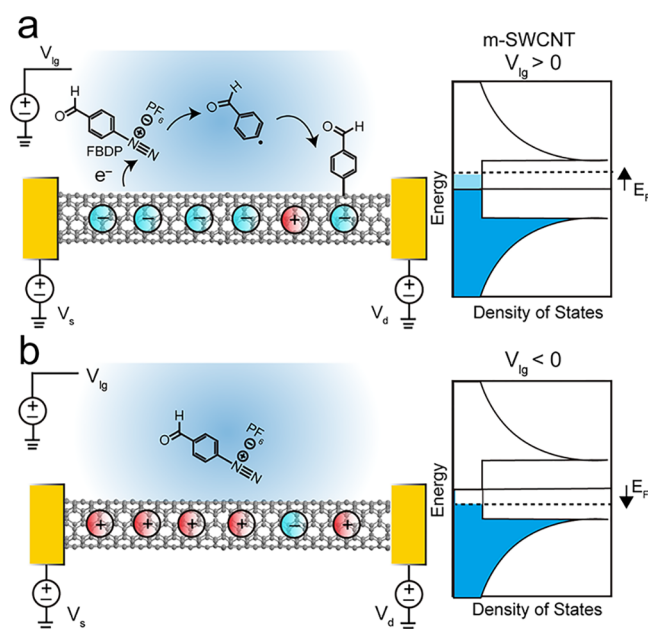
are subsequently investigated with scanning electron microscopy (SEM). As a result, $13.1 \pm 3.9\%$ of the total electrodes show both single and conducting nanotube bridges, corresponding to approximately 36 devices per chip. This yield is lower than the yield from SEM inspection alone (25%) because a CNT bridging an electrode pair can be imperfectly contacted, which is difficult to detect in an SEM image.

After initial electrical characterization, several chips containing tens of working CNTFET devices are wire-bonded to land-grid array (LGA) packages to interface with a custom printed circuit board (Figures S4 and S5, Supporting Information). Once a microfluidic chamber is attached to the chip surface, aqueous buffer solution ($100\ \text{mM}$ sodium phosphate buffer at $\text{pH}\ 8.0$) is introduced. I – V characteristics are measured by varying the liquid-gate potential (V_{lg}) set by a Pt electrode relative to the source potential of the device (Figure 2b). The peak current levels (between 10 and $1000\ \text{nA}$) for spin-cast devices are comparable to those previously reported for CVD-grown carbon nanotube devices with similar CNT length.^{30,31} We attribute much of the observed variance in the conductance to variance in tube diameters and chirality as well as defects that may be introduced into the tubes in the purification and suspension processes, described in more detail below. Additional characterization, including low-frequency noise spectra, appears in the Supporting Information (Figures S6 and S7). We favor m-SWCNT for these studies because

devices showing measurable conductance over the wide V_{lg} range allow for more detailed application of electronic melting³² as well as the optimization of gate-dependent SNR.³²

Controlled Diazonium Point Functionalization. Building on recent studies suggesting the ability to control the number of stable sp^3 defects on a carbon nanotube in aryl diazonium addition with bias,²⁵ we expose the spin-cast devices to 4-formylbenzene diazonium hexafluorophosphate (FBDP), which generates an aldehyde group after the reaction.³³ The extent of electron transfer, which leads to the formation of aryl radicals, is dependent on the electron density near the Fermi energy of the carbon nanotube. Hence, the diazonium reactivity is controlled through the applied V_{lg} , which modulates this Fermi level (Scheme 1).

Scheme 1. Illustration of V_{lg} -Induced Diazonium Reaction on the CNTFET^a



^a4-Formylbenzene diazonium hexafluorophosphate (FBDP) is employed as the substituent. The hexafluorophosphate (PF_6) counterion provides stability to the FBDP molecule. An aldehyde group opposite to the diazonium cation is used for DNA conjugation. (a) When V_{lg} is positive relative to the CNT surface, the Fermi level (E_F) of the m-SWCNT is shifted up, promoting sp^3 defect generation by donating the electrons to the positively charged N_2 group of the FBDP to form an aryl radical. (b) When V_{lg} is negative, E_F is shifted down, halting the reaction as the population of electrons near the Fermi level is reduced.

To study the effects of the applied V_{lg} on reaction kinetics in our system, we show current–time (I – t) recordings (collected at 25 kSps) of two representative spin-cast devices with a fixed V_{lg} of -500 mV and 0 V in the presence of FBDP solution at micromolar concentrations (Figure 3). Flicker noise is also evident in these traces, which is characteristic of these devices (Figure S8, Supporting Information).^{30,34} At V_{lg} of -500 mV, a m-SWCNT device exhibits a single current level with no discernible current drops for the entire recording time (515 s) after FBDP exposure (Figure 3a). We attribute this to the fact that the diazonium reaction is inhibited at this V_{lg} by making holes the dominant charge carrier in the CNTs. However, another m-SWCNT device with fixed V_{lg} at 0 V exhibits

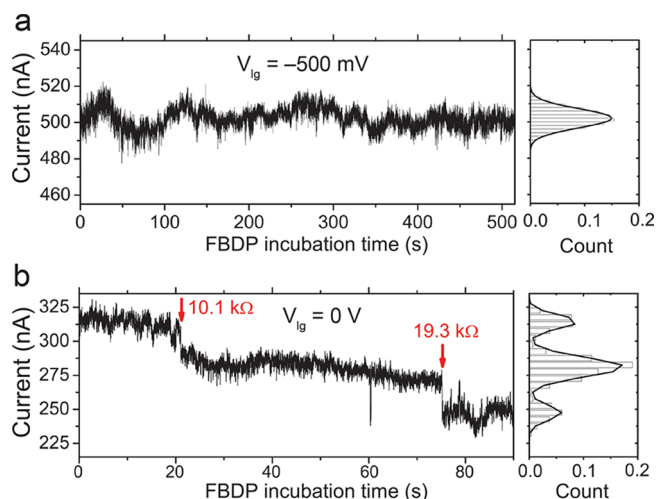


Figure 3. Liquid gate potential dependent diazonium reaction. (a) One representative I – t trace (515 s) of one m-SWCNT device after introduction of $72 \mu\text{M}$ FBDP solution (at $t = 0$). V_{lg} is fixed at -500 mV and V_{sd} of 50 mV is applied. One conductance level is evident, and the corresponding current histograms show a single Gaussian distribution. (b) Representative I – t trace (90 s) of another m-SWCNT device after introduction of $10 \mu\text{M}$ FBDP solution, while V_{sd} of 50 mV and V_{lg} of 0 V are fixed. Red arrows indicate times at which discrete downward current steps are observed. Corresponding histograms of current show that the current drops are clearly quantized. Counts of the histogram are normalized by dividing by the sum of the total counts. Data in the I – t trace graphs are sampled at 10 ms intervals from 1 kHz raw data.

discrete current levels 90 s after FBDP exposure (Figure 3b). Histograms characterizing the I – t recordings of the device report two discrete, resolved current levels. In this experiment, the initial resistance of the device was 128.0 k Ω at V_{lg} of -500 mV before introducing FBDP, and the resistance changes (ΔR) associated with the two current drops were quantified as 10.1 k Ω for the first drop and 19.3 k Ω for the second on a m-SWCNT.

To confirm that these stepwise current drops originate from the diazonium reaction, I – t characteristics of the device were also monitored with the introduction of a nondiazonium agent, 4-aminobenzaldehyde, in which the N_2 group of the FBDP is replaced by an amine group (Figure S9, Supporting Information). As the V_{lg} of the m-SWCNT device was positively increased from -500 to $+200$ mV, discrete steps in current were not observed during the nondiazonium agent exposure, and there was no significant change in conductance before and after exposure (3.8%). In the case of the FBDP treatment, however, two current steps were detected after V_{lg} was reached at -200 mV. The current rapidly decreased as V_{lg} was increased further, causing a large decrease in conductance (89.9%) after the experiment. It indicates that the m-SWCNT was heavily defected as a result of the diazonium reaction.

By keeping V_{lg} fixed at -500 mV during FBDP exposure, sp^3 defect generation could be avoided for an m-SWCNT device. Exposure to FBDP, however, does result in a larger conductance change (8.2%) compared to the change observed with a nondiazonium agent treatment (Figure S10, Supporting Information). Although stringent washing steps were performed after FBDP treatment, we attribute this conductance change to residual charges from diazonium salt absorbed to the CNT sidewall and doping the channel.³⁵ These conductance

Table 1. Representative Device Summary for Three Chips

device	device type	initial resistance ($k\Omega$)	threshold potential (mV)	no. of resistance steps	ΔR values ($k\Omega$)	single-molecule DNA activity
A1	m-SWCNT	122.7	50	2	31.6 34.4	yes
A2	m-SWCNT	89.5	200	1	8.7	no
B3	m-SWCNT	97.8	-50	2	1.6 1.4	yes
B4	m-SWCNT	657.7	400	2	311.6 501.6	no
B5	m-SWCNT	149.8	-100	1	9.7	yes
B6	s-SWCNT	923.6	300	0		no
B7	s-SWCNT	155.7	300	0		no
C8	m-SWCNT	114.6	200	1	9.4	no
C9	s-SWCNT	530.3	100	1	124.1	no
C10	s-SWCNT	822.9	100	1	128.0	yes

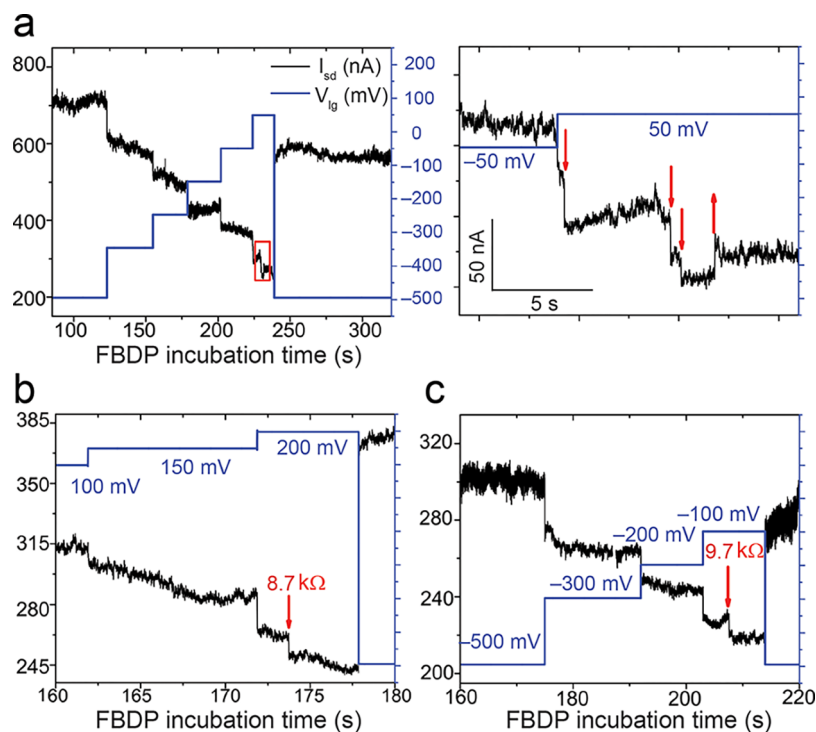


Figure 4. Feedback-controlled diazonium reaction for single-point functionalization. Initially liquid gate potential (V_{lg}) of -500 mV is applied and subsequently increased to promote the reaction. When a downward current step is detected, V_{lg} is immediately switched back to -500 mV to halt the reaction. Overlaid $I-t$ and $V_{lg}-t$ records of device A1 during FBDP exposure, in which a device is exposed to $72 \mu\text{M}$ FBDP solution at V_{sd} of 100 mV (a; left). Zoomed-in view of the red box in the threshold reaction potential, in which three consecutive downward steps and one upward step are monitored while holding V_{lg} at 50 mV for approximately 15 s, indicating two ultimate sp^3 defects (a; right). Overlaid time traces of single-point-functionalized devices. Device A2 in (b) is exposed to $72 \mu\text{M}$ FBDP solution at V_{sd} of 50 mV. A current step corresponding to $8.7 k\Omega$ is observed when V_{lg} reaches 200 mV. Device B5 in (c) is exposed to $6 \mu\text{M}$ FBDP solution at V_{sd} of 50 mV. A single downward current step results in a resistance change of $9.7 k\Omega$ to the nanotube after V_{lg} reaches -100 mV. No further current steps are observed after setting V_{lg} to -500 mV. Data in the $I-t$ trace graphs are sampled at 10 ms intervals from 1 kHz raw data.

changes can be clearly differentiated from the change due to sp^3 defect generation since chemical doping does not alter the conductance at the neutrality point.

We further utilized the V_{lg} -controlled diazonium reaction to create single sp^3 defects. During the FBDP incubation, V_{lg} (which begins at -500 mV) for each individual device is increased by $+50$ mV steps every 10 s until one discrete downward step of current is detected. Within 10 s after this defect generation is detected, V_{lg} is switched back to -500 mV to halt further reactions. Device conductance is continuously monitored (while holding V_{lg} at -500 mV) until the FBDP

solution is flushed from the device to ensure that the single defect status remains unchanged as residual reagent is purged. Table 1 summarizes the results on a representative set of devices for which controlled functionalization was performed, including both metallic and semiconducting tubes and different numbers of controlled conductance steps during the FBDP reaction. In addition, several devices are included that had no stepwise drops of current during FBDP exposure. The initial device resistance before the FBDP treatment, the value of V_{lg} at which defect generation is first observed (threshold potential), and the ΔR step values are all noted. We note that all of these

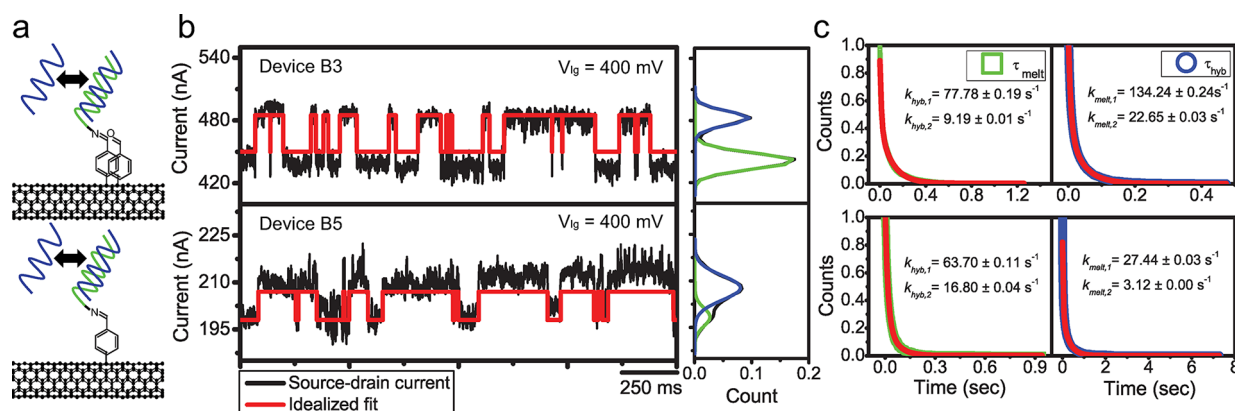


Figure 5. Verifying the application of point-functionalized CNTFETs by sensing DNA melting dynamics. (a) Probe DNA (green) shown tethered to a two-point-functionalized device (top, device B3) and a single-point-functionalized device (bottom, device B5). After tethering probe DNA to the defect site, the solution containing fully complementary target DNA (colored in blue, 100 nM) is introduced to the devices at a fixed temperature (40 °C) while holding V_{lg} at 400 mV. (b) $I-t$ measurements ($V_{sd} = 100$ mV) for each device. The total recording time is 180 s, and a representative 2 s length trace of the raw source-drain current (colored in black) is overlaid with an idealized fit (colored in red). Corresponding histograms of the two devices are plotted by counting the current in 60 s length traces (colored in black) which are fit by two Gaussian distributions. Counts of the histogram are normalized by dividing by the sum of the total counts. (c) Plots of the dwell time of the lower conductance state (green) and the high conductance state (blue) are constructed from the idealized trajectories for the total recorded length (180 s) and fit with a double-exponential function (red), yielding the rates of hybridization (k_{hyb}) and melting (k_{melt}). For the analysis of Device B3, the r -squared value of k_{hyb} and k_{melt} are 0.998 and 0.999, respectively. In case of device B5, the r -squared value of k_{hyb} and k_{melt} are 0.999 and 0.996, respectively.

nondefected devices show p-type semiconducting electrical properties, while most of the functionalized devices exhibit metallic characteristics (six out of eight devices). In particular, m-SWCNTs are better able to stabilize the transition state through electron donation and are consequentially more reactive in aryl-radical reactions due to their finite electron density at the Fermi level.^{36,37}

As expected, the nonfunctionalized p-type s-SWCNT device in Table 1 (device B7) showed an average conductance change of 0.05% in $I-V_{lg}$ characteristics after FBDP exposure. The two-point functionalized device (device B4) and the single-point functionalized device (device B5) each exhibited average conductance changes of 45.8% and 46.3% after FBDP treatment, respectively (Figure S11, Supporting Information).

Electrochemical surveillance of the reaction can also detect unstable or reverse reactions on the CNT sidewall. In one functionalization trial (device A1), we were able to detect one upward current step after three serial stepwise drops induced at V_{lg} of 50 mV indicating a detachment of the unstable isolated aryl defect (Figure 4a). Desorption of isolated aryl group is possible if a remaining radical localizes near the defect site.³⁸ Indeed, we were able to discern a rapid transition of current indicating diffusion and desorption dynamics of a short-lived single defect (Figure S12, Supporting Information). This unstable aryl radical promotes a second reaction to form stable aryl pairs when electrons are donated from the carbon nanotube. Most defect generation reactions resulted in stable products. Representative stable single-defected devices are shown in Figure 4b (device A2) and Figure 4c (device B5). A single downward step for the first (second) device, corresponding to the resistance change of 8.7 k Ω (9.7 k Ω), is detected within a few seconds after V_{lg} reaches 200 mV (−100 mV). Subsequent downward or upward steps are not observed after this single defect generation.

To understand the change in resistance associated with the creation of sp^3 defects, we quantified the first resistance step observed from each of 13 devices and found that the resulting

values were positively correlated with the initial device resistance (Figure S13, Supporting Information). The initial device resistance in excess of the contact resistance provides a good estimate of the density of intrinsic defects in the CNT channel. For the 10 devices with low initial resistance (109.3 ± 24.2 k Ω), we attribute most of this resistance to the Ti contacts.³⁹ For these devices, the average resistance change for sp^3 defect generation was approximately 9.8 k Ω . The other three devices exhibited higher initial resistance (670.3 ± 146.7 k Ω) due to a higher density of intrinsic defect in the CNT channel, likely introduced during the purification and suspension processes.⁴⁰ In this case, carrier transport becomes more localized, resulting in much larger resistance changes for single sp^3 defect generation.⁴¹ As expected, these devices showed much larger resistance steps (187.9 k Ω) for single sp^3 defect generation.

Estimation of Conjugation Yield by Sensing Single-Molecule DNA-Melting Dynamics. To demonstrate the functioning of the spin-cast CNTFETs as single-molecule transducers, the single sp^3 defect sites created in each device (Table 1) are covalently conjugated to an amine-modified 20-mer single-stranded DNA (ssDNA). We note that since spin-cast deposition results in surface-bound CNT devices, substrate charge trap induced RTS can occur.³⁰ Devices displaying significant RTS are excluded from further use.

In previous studies, we demonstrated that smFETs are capable of characterizing DNA hybridization and melting kinetics by temporal analysis of the resulting RTS and that a positive V_{lg} is able to promote the molecular dissociation. RTS is observed with two discrete conductance levels (high and low) which correspond to the hybridized and melted state of the probe molecule, respectively.⁵

We perform a similar experiment here to validate single-molecule sensing capabilities of the devices fabricated. After the 20-mer probe DNA is tethered to the defect site, a solution containing fully complementary target DNA (100 nM) is introduced at a fixed temperature (40 °C) (Figure 5a), close to

the theoretical melting temperature of $T_m = 49.7$ °C. Previous studies found that the electrostatic force induced by a positive V_{lg} lowers the effective melting temperature, decreasing the DNA hybridization rate (k_{hyb}) and increasing DNA melting rate (k_{melt}). $I-t$ series are monitored at several liquid gate potential (V_{lg}) to modulate DNA dissociation dynamics. $I-t$ traces for two different devices, one having two defects (device B3) and one having a single defect site (device B5), are independently monitored, and active RTS is detected at V_{lg} of 400 mV (Figure 5b). The histograms of 60 s $I-t$ traces show two distinct conductance levels. In contrast, only one conductance level (and no RTS) is evident in two control experiments, one in which no target DNA is present and one in which a noncomplementary 20-mer target DNA is present (Figure S14, Supporting Information).

An idealized trace, resulting from fits to the raw data using an iterative detection algorithm,⁴² is used for subsequent temporal analysis. $I-t$ traces are fit to a two-state model to determine dwell times in the hybridized (τ_{hyb}) and melted states (τ_{melt}). A double-exponential fit to the resulting histograms determines the rate constants k_{hyb} and k_{melt} . k_{hyb} is mainly determined by the diffusion of target to the probe and is a strong measure of target concentration. This diffusion process can be one-dimensional (1D) along the channel or three-dimensional (3D) from solution to the device.⁴³ For the 100 nM concentration, the faster k_{hyb} corresponds to the 3D diffusion (Figure 5c) and is used in subsequent analysis. The two different k_{melt} values are also associated with 1D and 3D diffusion, in which the faster corresponds to 3D diffusion and is chosen for subsequent analysis. Our previous study revealed that the equilibrium constant (K_{eq}), determined by calculating the ratio of k_{hyb} to k_{melt} , is close to one at V_{lg} of 400 mV for the fully complementary target DNA at 40 °C. Here, the resulting K_{eq} values are in good agreement with the estimation.⁵

The Schiff base reaction between the amine-modified ssDNA probe and aldehyde group of FBDP also has a finite yield. As a result, a two-point-functionalized device can tether two, one, or no probes. Device B3 in Figure 5, which has two defect sites, for example, shows only two discrete conductance states in the presence of fully complementary target DNA solution. In contrast, another two-point functionalized device A1 (Figure S15, Supporting Information) shows RTS with at least three states. These multiple conductance state transitions are attributed to the fact that two probe DNAs are attached to the device.

CONCLUSIONS

We have developed a manufacturable fabrication process for CNTFETs by spin-casting low densities of single-walled carbon nanotubes from an aqueous suspension onto 100 mm silicon substrates. Uniform spin-coating is achieved on these wafers, allowing for large-scale manufacturing of CNTFET arrays. We have also demonstrated a protocol for controlled single-point functionalization using diazonium salt chemistry. By tethering a single DNA probe molecule, point-functionalized nanotubes function as all-electronic single-molecule transducers, smFETs, showing exquisite sensitivity to the increased nearby charge that results from hybridization of a complementary DNA strand. Efforts to expand the approach to 300 mm wafers and smFET arrays on active complementary metal-oxide-semiconductor substrates will accelerate the development of diagnostic platforms. Such arrays have the potential to allow genomic material to be assayed at

concentrations comparable to that achieved by quantitative polymerase chain reaction while enabling heavily multiplexed assays similar to what is possible with microarrays.

METHODS

Nanotube Suspensions. Stock aqueous nanotube suspensions (Super PureTubes) with an average diameter ranging from 1.2 to 1.7 nm were purchased from NanoIntegris, Inc. These nanotubes are suspended in deionized H₂O with sodium cholate hydrate as the surfactant.

100 mm Wafer Device Fabrication. A stock solution with a nanotube concentration of 250 μ g/mL is sonicated before dilution and spin-coating on 100 mm Si/SiO₂ wafers with a 500 μ m heavily p-doped silicon substrate and 285 nm of thermally grown silicon dioxide (Figure S2, Supporting Information).⁴⁴ These wafers have been pretreated with oxygen plasma for 30 s to promote surface wetting of the solvent. One to two milliliters of solution is dispensed. The resulting suspension is spun using a two-step process: 400 and 100 rpm/second for 15 s, followed by 3000 rpm and 10000 rpm/second for 45 s. Bilayer resist is spun (DS-K101-312 antireflective coating at 5000 rpm for 1 min, followed by UV210-0.3 at 2500 rpm for 1 min) and exposed using a DUV stepper. After spinning the CNTs, titanium (50 nm) is deposited to create 280 pairs of 20 μ m wide source and drain electrical contacts separated by 0.5 μ m in each reticle. Areas for platinum electrode bars, serving as pseudoreference electrodes, are patterned on either side of the electrode array; 75 nm Pt is deposited in these areas. This reticle is stepped across the wafer, yielding 45 1 \times 1.1 cm² dice. Gold bond pads are also patterned for device packaging. Au (90 nm) is deposited in these regions, and then a photoresist is patterned on the wafer to protect nanotubes transiting the electrodes. The wafer is exposed to O₂ plasma (50 W at 30 mT for 60 s), resulting in nanotubes being etched away from the regions outside the electrode gap. Subsequently, additional photoresist covers the entire area of the wafer to protect the surface, and the wafer is cut into 45 chips. Individual chips are separated from the wafer, and the photoresist is stripped. Chips are then annealed in vacuum at 425 °C for 15 min.

Current–Voltage ($I-V_{bg}$) Characterization in Air. Conductive devices are screened by taking the current–voltage ($I-V$) characteristics of individual 280 electrode pairs in air using a semiconductor parameter analyzer (Agilent 4155C). Current–voltage ($I-V$) responses are performed by applying an alternating back-gated voltage sweep with the step size of 500 mV and measuring the current at the same time at each voltage. With constant source–drain voltages (V_{sd}) of 100 mV for each chip, the back-gate voltage (V_{bg}), applied to the heavily doped p⁺⁺ silicon substrate, is swept from -10 to $+10$ V.

SEM Imaging. SEM images are taken by Zeiss Sigma VP FESEM. Images are captured only at electrode sites which exhibit significant current response based on the current–voltage ($I-V$) characteristics.

Measurement Setup. Single-crossing CNT devices and platinum pads on a chip are selectively connected to a land-grid array (LGA) package using an automated wire bonder (Kulicke & Soffa) and subsequently placed onto a custom-made printed circuit board (PCB). The measurement setup consists of a polydimethylsiloxane (PDMS) microfluidic channel for interfacing solution with the fully fabricated devices, a custom-made PCB for data acquisition (see Figures S4 and S5, Supporting Information)⁵ and a temperature controller for maintaining and modulating the temperature near the chip surface. The microfluidic system with temperature controller is responsible for delivering samples, exchanging samples, and performing washes during the experiment. The PDMS microfluidic channel has the dimensions: 7 mm long, 750 μ m wide, and approximately 500 μ m tall. Inlet and outlet holes are punched into the channel, and two sterile tubing segments are inserted. A syringe pump connected to the outlet terminal withdraws fluid exiting the channel, thus allowing full control over flow rates. The circuit board contains 58 independently addressable measurement channels that are simultaneously interrogated in real-time. The circuitry for each channel incorporates tunable drain and source potentials and is composed of two gain

stages: a front-end trans-impedance amplification stage with a fixed resistive gain of $1\text{ M}\Omega$, followed by an inverting voltage amplifier with variable gain from 2 to $200\times$. Each channel furthermore utilizes a second-order antialiasing filter topology, limiting the signal bandwidth to approximately 5.3 kHz. Readings from each channel are sampled at a rate of 25 kSps. Temperature is controlled inside a custom acrylic enclosure with three parallel resistive silicone heaters (12 V_{max}) and one miniature fan mounted near the top. A thermocouple is inserted near the bottom to monitor the temperature close to the microfluidic cell stamped on the chip.

Current Liquid Gate Potential ($I-V_{\text{lg}}$) Characterization in an Aqueous solution. $I-V_{\text{lg}}$ characteristics in an aqueous phosphate buffer solution (100 mM, pH 8.0) are measured in a PDMS microfluidic channel. With the source-drain voltage (V_{sd}) of 50 mV, the liquid gate potential (V_{lg}) relative to the pseudoreference Pt electrodes is applied from -500 to $+500$ mV at intervals of 50 mV. The measurement time for the current is 1 s at each V_{lg} , and three successive $I-V_{\text{lg}}$ sweeps are performed to produce $I-V_{\text{lg}}$ plots. The conductance changes are estimated by calculating the average difference of current at each V_{lg} point.

Single Diazonium Functionalization to Individual CNT Devices. 4-Formylbenzene diazonium hexafluorophosphate (FBDP) is synthesized using a previously established protocol.³³ FBDP is diluted in buffer solution (100 mM sodium phosphate buffer pH 7.0), and FBDP concentrations between 6.0 and $72.0\text{ }\mu\text{M}$ are chosen to allow for real-time observation. $I-V_{\text{lg}}$ characteristics and current–time ($I-t$) recording are measured with a constant source-drain voltages (V_{sd}) of 50 mV or 100 mV for each chip. Before introducing the FBDP solution, $I-V_{\text{lg}}$ characteristics are taken with the PDMS microfluidic channel filled with sodium phosphate buffer (100 mM, pH 8.0). After that, the $I-t$ recording is performed before, during, and after diazonium reaction. After completion of the reaction, an $I-V_{\text{lg}}$ measurement is performed again.

Probe DNA Conjugation. After the functionalization step, the chip is exposed to $10\text{ }\mu\text{M}$ of amine-terminated probe DNA ($5' \text{-NH}_2\text{-CTGTGATTTCAAATTCAGTG-3'}$) diluted in a buffer solution (100 mM sodium phosphate buffer pH 7.0) containing $200\text{ }\mu\text{M}$ sodium cyanoborohydride (NaBH_3CN) dissolved in 1 M NaOH which is used for the reduction of the Schiff base to a covalent bond. The chip is incubated in the probe DNA solution at room temperature overnight. Following this incubation step, the temperature of the measurement system is increased to $40.0\text{ }^\circ\text{C}$, and the probe DNA solution is washed out with buffer solution at the flow rate of $25\text{ }\mu\text{L}/\text{min}$ for 45 min.

Monitoring DNA Melting Dynamics. The target DNA sequences are composed of a fully complementary 20-mer ($5' \text{-CACTGAATTTGAAATCACAG-3'}$). All experiments are performed in 43 mM aqueous phosphate buffer (pH 8.0) with fully complementary DNA target at a concentration of 100 nM. Noncomplementary DNA ($5' \text{-GTGATTTCACCTTGCAATGTC-3'}$) at the same concentration is used as a negative control. Each current–time ($I-t$) trajectory is recorded for 180 s at a fixed temperature (40 and $50\text{ }^\circ\text{C}$) over a range of V_{lg} . To reuse the devices, the chip is washed with buffer at a flow rate of $25\text{ }\mu\text{L}/\text{min}$ for 45 min after adjusting the system temperature to $50\text{ }^\circ\text{C}$ to melt DNA duplexes.

Data Analysis. Raw transient current data are digitally filtered with a fourth-order Butterworth filter with a cutoff frequency of 1 kHz. The resulting data are further analyzed using an iterative event detection algorithm which assumes a two-state model, written initially to analyze nanopore blockade currents.⁴² This algorithm compensates for $1/f$ noise common to nanotube conductance signals by tracking and subtracting out a wandering baseline. Idealized traces, resulting from fits to the raw data in the iterative detection algorithm, are used to extract information about single-molecule binding kinetics.

ASSOCIATED CONTENT

Supporting Information

The Supporting Information is available free of charge on the ACS Publications website at DOI: 10.1021/acsnano.8b03073.

Figure S1–S15, including additional CNT electrical characterization, FBDP defect generation comparisons, and negative controls for DNA sensing (PDF)

AUTHOR INFORMATION

Corresponding Author

*E-mail: shepard@ee.columbia.edu.

ORCID

Yoonhee Lee: 0000-0003-0680-7668

Scott M. Trocchia: 0000-0002-7553-5208

Author Contributions

[†]Y.L. and S.M.T. contributed equally.

Notes

The authors declare no competing financial interest.

ACKNOWLEDGMENTS

We acknowledge R. Brown of the Cornell Nanofabrication Facility for his fabrication insight and assistance. We also acknowledge B. Vanhorenbeke and D. Bouilly for useful discussions on preparing nanotube solutions and tuning spin parameters and J. Hon for assistance with data analysis procedures. Research reported in this publication was supported by the National Institute of Allergy and Infectious Diseases of the National Institutes of Health under Award No. U19AI109761, National Human Genome Research Institute of the National Institutes of Health under Award No. R01HG006882, and the National Institute of General Medical Sciences of the National Institutes of Health under Award No. R01GM107417.

REFERENCES

- (1) Wang, S. Z.; Vafabakhsh, R.; Borschel, W. F.; Ha, T.; Nichols, C. G. Structural Dynamics of Potassium-Channel Gating Revealed by Single-Molecule FRET. *Nat. Struct. Mol. Biol.* **2016**, *23*, 31–36.
- (2) Thoma, J.; Burmann, B. M.; Hiller, S.; Muller, D. J. Impact of Holdase Chaperones Skp and SurA on the Folding of Beta-Barrel Outer-Membrane Proteins. *Nat. Struct. Mol. Biol.* **2015**, *22*, 795–802.
- (3) Strunz, T.; Oroszlan, K.; Schafer, R.; Guntherodt, H. J. Dynamic Force Spectroscopy of Single DNA Molecules. *Proc. Natl. Acad. Sci. U. S. A.* **1999**, *96*, 11277–11282.
- (4) Qiu, R. Y.; DeRocco, V. C.; Harris, C.; Sharma, A.; Hingorani, M. M.; Erie, D. A.; Weninger, K. R. Large Conformational Changes in MutS during DNA Scanning, Mismatch Recognition and Repair Signalling. *EMBO J.* **2012**, *31*, 2528–2540.
- (5) Vernick, S.; Trocchia, S. M.; Warren, S. B.; Young, E. F.; Bouilly, D.; Gonzalez, R. L.; Nuckolls, C.; Shepard, K. L. Electrostatic Melting in a Single-Molecule Field-Effect Transistor with Applications in Genomic Identification. *Nat. Commun.* **2017**, *8*, 15450.
- (6) Husale, S.; Persson, H. H. J.; Sahin, O. DNA Nanomechanics Allows Direct Digital Detection of Complementary DNA and MicroRNA Targets. *Nature* **2009**, *462*, 1075–1078.
- (7) Lee, Y.; Kim, Y.; Lee, D.; Roy, D.; Park, J. W. Quantification of Fewer than Ten Copies of a DNA Biomarker without Amplification or Labeling. *J. Am. Chem. Soc.* **2016**, *138*, 7075–7081.
- (8) Plochowitz, A.; Crawford, R.; Kapanidis, A. N. Characterization of Organic Fluorophores for *in vivo* FRET Studies based on Electroporated Molecules. *Phys. Chem. Chem. Phys.* **2014**, *16*, 12688–12694.
- (9) Shaner, N. C.; Steinbach, P. A.; Tsien, R. Y. A Guide to Choosing Fluorescent Proteins. *Nat. Methods* **2005**, *2*, 905–909.
- (10) Dong, M. D.; Sahin, O. A Nanomechanical Interface to Rapid Single-Molecule Interactions. *Nat. Commun.* **2011**, *2*, 247.
- (11) Stroh, C.; Wang, H.; Bash, R.; Ashcroft, B.; Nelson, J.; Gruber, H.; Lohr, D.; Lindsay, S. M.; Hinterdorfer, P. Single-Molecule

Recognition Imaging-Microscopy. *Proc. Natl. Acad. Sci. U. S. A.* **2004**, *101*, 12503–12507.

(12) Singh, P.; Campidelli, S.; Giordani, S.; Bonifazi, D.; Bianco, A.; Prato, M. Organic Functionalisation and Characterisation of Single-Walled Carbon Nanotubes. *Chem. Soc. Rev.* **2009**, *38*, 2214–2230.

(13) Sorgenfrei, S.; Chiu, C. Y.; Johnston, M.; Nuckolls, C.; Shepard, K. L. Debye Screening in Single-Molecule Carbon Nanotube Field-Effect Sensors. *Nano Lett.* **2011**, *11*, 3739–3743.

(14) Stern, E.; Wagner, R.; Sigworth, F. J.; Breaker, R.; Fahmy, T. M.; Reed, M. A. Importance of the Debye Screening Length on Nanowire Field Effect Transistor Sensors. *Nano Lett.* **2007**, *7*, 3405–3409.

(15) Warren, S. B.; Vernick, S.; Romano, E.; Shepard, K. L. Complementary Metal-Oxide-Semiconductor Integrated Carbon Nanotube Arrays: Toward Wide-Bandwidth Single-Molecule Sensing Systems. *Nano Lett.* **2016**, *16*, 2674–2679.

(16) Bouilly, D.; Hon, J.; Daly, N. S.; Trocchia, S.; Vernick, S.; Yu, J.; Warren, S.; Wu, Y.; Gonzalez, R. L.; Shepard, K. L.; Nuckolls, C. Single-Molecule Reaction Chemistry in Patterned Nanowells. *Nano Lett.* **2016**, *16*, 4679–4685.

(17) Choi, Y.; Moody, I. S.; Sims, P. C.; Hunt, S. R.; Corso, B. L.; Perez, I.; Weiss, G. A.; Collins, P. G. Single-Molecule Lysozyme Dynamics Monitored by An Electronic Circuit. *Science* **2012**, *335*, 319–324.

(18) Zhang, X.; Chenet, D.; Kim, B.; Yu, J.; Tang, J. Z.; Nuckolls, C.; Hone, J. Fabrication of Hundreds of Field Effect Transistors on a Single Carbon Nanotube for Basic Studies and Molecular Devices. *J. Vac. Sci. Technol., B: Nanotechnol. Microelectron.: Mater., Process., Meas., Phenom.* **2013**, *31*, 06F101.

(19) Chen, R. J.; Zhang, Y. G.; Wang, D. W.; Dai, H. J. Noncovalent Sidewall Functionalization of Single-Walled Carbon Nanotubes for Protein Immobilization. *J. Am. Chem. Soc.* **2001**, *123*, 3838–3839.

(20) Kulkarni, G. S.; Zhong, Z. H. Detection beyond the Debye Screening Length in a High-Frequency Nanoelectronic Biosensor. *Nano Lett.* **2012**, *12*, 719–723.

(21) Banerjee, S.; Hemraj-Benny, T.; Wong, S. S. Covalent Surface Chemistry of Single-Walled Carbon Nanotubes. *Adv. Mater.* **2005**, *17*, 17–29.

(22) Allongue, P.; Delamar, M.; Desbat, B.; Fagebaume, O.; Hitmi, R.; Pinson, J.; Saveant, J. M. Covalent Modification of Carbon Surfaces by Aryl Radicals Generated from the Electrochemical Reduction of Diazonium Salts. *J. Am. Chem. Soc.* **1997**, *119*, 201–207.

(23) Coleman, K. S.; Bailey, S. R.; Fogden, S.; Green, M. L. H. Functionalization of Single-Walled Carbon Nanotubes via the Bingel Reaction. *J. Am. Chem. Soc.* **2003**, *125*, 8722–8723.

(24) Stevens, J. L.; Huang, A. Y.; Peng, H. Q.; Chiang, L. W.; Khabashesku, V. N.; Margrave, J. L. Sidewall Amino-Functionalization of Single-Walled Carbon Nanotubes through Fluorination and Subsequent Reactions with Terminal Diamines. *Nano Lett.* **2003**, *3*, 331–336.

(25) Wilson, H.; Ripp, S.; Priscy, L.; Brown, M. A.; Sharf, T.; Myles, D. J. T.; Blank, K. G.; Minot, E. D. Electrical Monitoring of sp^3 Defect Formation in Individual Carbon Nanotubes. *J. Phys. Chem. C* **2016**, *120*, 1971–1976.

(26) Lee, Y. S.; Nardelli, M. B.; Marzari, N. Band structure and Quantum Conductance of Nanostructures from Maximally Localized Wannier Functions: the Case of Functionalized Carbon Nanotubes. *Phys. Rev. Lett.* **2005**, *95*, 076804.

(27) Kim, Y.; Minami, N.; Zhu, W. H.; Kazaoui, S.; Azumi, R.; Matsumoto, M. Langmuir-Blodgett Films of Single-Wall Carbon Nanotubes: Layer-by-Layer Deposition and In-Plane Orientation of Tubes. *Jpn. J. Appl. Phys.* **2003**, *42*, 7629–7634.

(28) Park, J. U.; Meitl, M. A.; Hur, S. H.; Usrey, M. L.; Strano, M. S.; Kenis, P. J. A.; Rogers, J. A. *In situ* Deposition and Patterning of Single-Walled Carbon Nanotubes by Laminar Flow and Controlled Flocculation in Microfluidic Channels. *Angew. Chem., Int. Ed.* **2006**, *45*, 581–585.

(29) Choi, S. J.; Bennett, P.; Takei, K.; Wang, C.; Lo, C. C.; Javey, A.; Bokor, J. Short-Channel Transistors Constructed with Solution-Processed Carbon Nanotubes. *ACS Nano* **2013**, *7*, 798–803.

(30) Sharf, T.; Wang, N. P.; Kevek, J. W.; Brown, M. A.; Wilson, H.; Heinze, S.; Minot, E. D. Single Electron Charge Sensitivity of Liquid-Gated Carbon Nanotube Transistors. *Nano Lett.* **2014**, *14*, 4925–4930.

(31) Franklin, A. D.; Chen, Z. H. Length Scaling of Carbon Nanotube Transistors. *Nat. Nanotechnol.* **2010**, *5*, 858–862.

(32) Heller, I.; Mannik, J.; Lemay, S. G.; Dekker, C. Optimizing the Signal-to-Noise Ratio for Biosensing with Carbon Nanotube Transistors. *Nano Lett.* **2009**, *9*, 377–382.

(33) Gavriluk, J.; Ban, H.; Nagano, M.; Hakamata, W.; Barbas, C. F. Formylbenzene Diazonium Hexafluorophosphate Reagent for Tyrosine-Selective Modification of Proteins and the Introduction of a Bioorthogonal Aldehyde. *Bioconjugate Chem.* **2012**, *23*, 2321–2328.

(34) Sharf, T.; Kevek, J. W.; Deborde, T.; Wardini, J. L.; Minot, E. D. Origins of Charge Noise in Carbon Nanotube Field-Effect Transistor Biosensors. *Nano Lett.* **2012**, *12*, 6380–6384.

(35) Farmer, D. B.; Golizadeh-Mojarad, R.; Perebeinos, V.; Lin, Y. M.; Tulevski, G. S.; Tsang, J. C.; Avouris, P. Chemical Doping and Electron-Hole Conduction Asymmetry in Graphene Devices. *Nano Lett.* **2009**, *9*, 388–392.

(36) Banerjee, S.; Wong, S. S. Selective Metallic Tube Reactivity in the Solution-Phase Osmylation of Single-Walled Carbon Nanotubes. *J. Am. Chem. Soc.* **2004**, *126*, 2073–2081.

(37) Lu, X.; Tian, F.; Feng, Y. B.; Xu, X.; Wang, N. Q.; Zhang, Q. N. Sidewall Oxidation and Complexation of Carbon Nanotubes by Base-Catalyzed Cycloaddition of Transition Metal Oxide: A Theoretical Prediction. *Nano Lett.* **2002**, *2*, 1325–1327.

(38) Margine, E. R.; Bocquet, M. L.; Blase, X. Thermal Stability of Graphene and Nanotube Covalent Functionalization. *Nano Lett.* **2008**, *8*, 3315–3319.

(39) Franklin, A. D.; Farmer, D. B.; Haensch, W. Defining and Overcoming the Contact Resistance Challenge in Scaled Carbon Nanotube Transistors. *ACS Nano* **2014**, *8*, 7333–7339.

(40) Cao, Q.; Han, S. J.; Tulevski, G. S.; Franklin, A. D.; Haensch, W. Evaluation of Field-Effect Mobility and Contact Resistance of Transistors That Use Solution-Processed Single-Walled Carbon Nanotubes. *ACS Nano* **2012**, *6*, 6471–6477.

(41) Sundqvist, P.; Garcia-Vidal, F. J.; Flores, F.; Moreno-Moreno, M.; Gomez-Navarro, C.; Bunch, J. S.; Gomez-Herrero, J. Voltage and Length-Dependent Phase Diagram of the Electronic Transport in Carbon Nanotubes. *Nano Lett.* **2007**, *7*, 2568–2573.

(42) Plesa, C.; Dekker, C. Data Analysis Methods for Solid-State Nanopores. *Nanotechnology* **2015**, *26*, 084003.

(43) Sorgenfrei, S.; Chiu, C. Y.; Gonzalez, R. L., Jr.; Yu, Y. J.; Kim, P.; Nuckolls, C.; Shepard, K. L. Label-Free Single-Molecule Detection of DNA-Hybridization Kinetics with a Carbon Nanotube Field-Effect Transistor. *Nat. Nanotechnol.* **2011**, *6*, 126–132.

(44) Vichchulada, P.; Cauble, M. A.; Abdi, E. A.; Obi, E. I.; Zhang, Q. H.; Lay, M. D. Sonication Power for Length Control of Single-Walled Carbon Nanotubes in Aqueous Suspensions Used for 2-Dimensional Network Formation. *J. Phys. Chem. C* **2010**, *114*, 12490–12495.